TECHNISCHE MECHANIK
an open access journal

journal homepage: www.ovgu.de/techmech

Tech. Mech., Vol. 40, Is. 2, (2020), 175–190

Received: 29.11.2019
Accepted: 23.07.2020
Available online: 27.07.2020

RVE-size Estimation and Efficient Microstructure-based Simulation of Dual-Phase Steel

Frederik Scherff[1,3]*, Jessica Gola[2,3], Sebastian Scholl[3], Kinshuk Srivastava[3], Thorsten Staudt[3], Dominik Britz[2], Frank Mücklich[2], and Stefan Diebels[1]

[1] Universität des Saarlandes, Lehrstuhl für Technische Mechanik, Campus A4.2, 66123 Saarbrücken, Germany
[2] Universität des Saarlandes, Lehrstuhl für Funktionswerkstoffe, Campus D3.3, 66123 Saarbrücken, Germany
[3] AG der Dillinger Hüttenwerke, Werkstraße 1, 66763 Dillingen, Germany

Abstract: Dual-phase steel shows a pronounced structure-property correlation, caused by its internal structure consisting of a soft ferrite matrix and embedded hard martensite regions. Due to its high strength combined with high ductility, dual-phase steel is particularly suitable for energy-absorbing and strength-relevant sheet metal applications, but its use as heavy plate is also desirable. Due to the complex microstructure, microstructure-based simulation is essential for a realistic simulation of the mechanical properties of dual-phase steel. This paper describes two important points for the microstructure-based simulation of dual-phase steel. First a method for the straightforward experimental estimation of the RVE size based on hardness measurements prior to tomography preparation is presented and evaluated. Secondly, a method for the efficient meshing of these microstructures, based on material definition at the integration points of a finite element model, is developed.

Keywords: dual-phase steel, RVE size, FEM, 3D tomography, MatIP

1 Introduction

Steel is one of the most widely used structural materials; for example, in 2017 its production amount exceeded the production amount of all plastics by a factor of more than five (PlasticsEurope (2017)). According to this large production amount, there is also a large variety of different steel classes, which differ in their exact internal structure and their properties. One of these classes is dual-phase steel, characterized by a two-phase microstructure of hard martensite regions embedded in a soft ferrite matrix. Due to its microstructure, the mechanical properties of dual-phase steel are defined by high strength and high ductility at the same time (Tasan et al. (2015)). Due to this performance profile, it is classically used in energy-absorbing, strength-relevant sheet metal components (Brands et al. (2016); Tarigopula et al. (2008)). At the same time, however, efforts to use dual-phase steel also in heavy plate products, for example in pipelines, are increasing (Ishikawa et al. (2015); Ji et al. (2014); Li et al. (2011)). The strong structure-property correlation of dual-phase steel makes microstructure-based simulations an important method for improving its mechanical properties and for adapting them to a specific application. The most important microstructural parameters influencing the properties of dual-phase steel are the quantity, shape and distribution of the martensite regions in the ferrite (Das and Chattopadhyay (2009); Davies (1978); Kang et al. (2007); Kim and Lee (2000); Tasan et al. (2015)). For this reason, simulations are used within the framework of the finite element method (FEM, (Zienkiewicz and Taylor (1977))) that explicitly include both phases of the dual-phase steel in the analysis. Simulations based on the real structure of the dual-phase steel have the advantage that they include the entire phase structure in the analysis. Therefore, no structural properties relevant for the macroscopic material properties are unintentionally neglected. By modelling the ferrite and martensite as discrete areas of the mesh, all microstructural details can be taken into account. Therefore simulations based on the real structure usually show a good agreement with the corresponding experiments (Dong et al. (2010); Katani et al. (2013); Marvi-Mashhadi et al. (2012); Paul (2013); Ramazani et al. (2014, 2013)).

For a microstructure based simulation, a 3D reconstruction of the material is required that is large enough to be representative for the material in terms of shape, distribution and connectivity. In the field of materials science, 3D reconstructions based on real structure of various, usually multi-phase materials are used to investigate the 3D microstructure. Tomography enables the microstructural characterization of a defined sample volume in contrast to two-dimensional surface characterization. Thus, important information about the formation and evolution of the phases can be obtained, which allows conclusions to be drawn about the properties of the material (Ohser and Mücklich (2000)). There are different methods that allow 3D reconstruction of a metallic material. Established methods that can be used to image large volumes include X-ray microcomputed tomography (µCT) (Desplentere et al. (2005); Yan et al. (2014); Zhou et al. (2018)) or serial sectioning tomography (Alkemper and Voorhees (2001); Keehan et al. (2008); Lasagni et al. (2007); Li et al. (1998); Mücklich et al. (2018); Roland et al. (2015)). At µCT the sample is irradiated with X-rays from many different directions and thus a three-dimensional image of the inner microstructure of the sample is computed (Buzug (2008)). In serial sectioning tomography a large number of two-dimensional microscopic images of the sample is recorded by removing a thin layer of the sample between the individual images. The two-dimensional

* E-mail address: s.diebels@mx.uni-saarland.de
doi: 10.24352/UB.OVGU-2020-024

images are then digitally combined to reconstruct the three-dimensional structure of the examined sample volume. A light optical serial sectioning tomography uses a light optical microscope to capture the image and the material is removed by mechanical polishing (Alkemper and Voorhees (2001); Li et al. (1998); Mücklich et al. (2018)). In case small cutting distances are required, a serial sectioning tomography can be performed using a focused ion beam (FIB) in a scanning electron microscope (SEM) (Burnett et al. (2016); Keehan et al. (2008); Lasagni et al. (2007); Li et al. (1998); Zhong et al. (2019)). However, not all 3D reconstruction methods are suitable for all metals, especially low alloyed, low carbon steels as investigated here. In case of steel, most transformation products are mostly iron, therefore showing a low atomic density contrast. A methodology that uses the material density contrast for the image acquisition, as the CT, can not be used. In addition, the resolution of CT depends on the observed volume. Very high resolutions can be achieved with small volumes. However, the resolution decreases with increasing volume of the sample (Fischer et al. (2011); Bauza et al. (2018)). Common FIB/SEM devices produce tomographies with a volume too small for the steels under consideration here (Brands et al. (2016); Mücklich et al. (2018)), but this issue can be overcome in specialized devices by adding a laser (Echlin and Pollock (2008)) or using other ion sources such as xenon (Burnett et al. (2016)) instead of gallium to increase the volume. In addition to the classical SEM images also other signals (e.g. EDS or EBSD) can be used for tomographies (Brands et al. (2016)). Another approach combines the advantages of classical serial sectioning tomography with images in SEM or EBSD (Uchic et al. (2016)). In comparison, the method of serial sectioning in combination with light microscopic images is widely used for steels. By contrasting the microstructures by etching, the different structure components can be separated (Britz et al. (2016)). For this reason, light optical serial sectioning tomography is still one of the most widely used methods for the production of large size steel tomography. Tomographies of two-phase steels with an edge length of 100-150 Âţm have already shown that the phases separated on 2D images have a high connectivity in 3D (Mücklich et al. (2015)).

The estimation of the size of the representative volume element (RVE) poses a particular challenge for simulations based on microstructures. The RVE describes the area of the microstructure that is just large enough to contain all relevant information about the microstructure (Hill (1963); Kanit et al. (2003); Tasan et al. (2014b)). A section of the microstructure with the size of the RVE thus shows the same microstructural properties at any point of the material. These properties additionally do not change for larger structural sections. Simulations on microstructure sections smaller than the RVE cannot reproduce the real macroscopic properties due to the scattering of the microstructure geometry depending on the location of the sampling. On one hand, simulations on microstructure sections larger than the RVE, on the other hand, require significantly more computing time and higher memory loads than necessary for simulation on a RVE due to the unnecessarily large geometry. The estimation of the RVE size is therefore a crucial point in the process of microstructure-based simulation. Nevertheless, the estimation of the RVE size is often carried out not at all (Katani et al. (2013); Paul (2013)) or only by time-consuming methods (Brands et al. (2016)). For these methods, a 3D tomography is carried out and it is compared to other tomographies of the same material or to the geometric parameters of a bigger micrograph of the sample. In this way, it can be determined, if the section is as big as or bigger than the RVE. If this is not the case, a new, bigger tomography has to be prepared. Therefore, methods to estimate the RVE's size before tomography preparation are desirable to save cost and time.

Tomographies with the size of a RVE often consist of tens of millions of voxels. This enormous size, coupled with the complex shape of the microstructure, poses difficulties for the simulation (Brands et al. (2016); Calcagnotto et al. (2010)). Due to the large number of elements, the computing time and the required amount of main memory considerably increases. In addition, unstructured geometry conforming meshing to reduce the number of elements of the FE mesh compared to the voxels of the tomography is very complex and only to a limited extent effective. In order to avoid these problems, simulations are often carried out only on the basis of two-dimensional structures in order to reduce the number of elements of the FE mesh and, in addition, the effort required to obtain the microstructure (Kadkhodapour et al. (2011); Paul (2013); Tasan et al. (2014b,a)). However, it has been shown that such two-dimensional simulations are not capable of correctly mapping the real material behavior (Diehl et al. (2016); Ramazani et al. (2013); Tasan et al. (2014a); Zeghadi et al. (2007)). As a result, three-dimensional simulations are indispensable despite the problems described. For this reason, straightforward methods of data reduction are needed to reduce the required computing time and memory load while preserving the microstructure information.

In the article two essential things for the correct microstructure-based simulation of dual-phase steel are presented. Due to the importance of the RVE, a straightforward experimental method for estimating the size of the RVE before the preparation of a tomography is described. It is based on the evaluation of different hardness indentations of the material. For an estimation of the RVE size based on the 3D microstructure, the first guess of the RVE size determines the size of the required tomography. Especially for an unexperienced experimentalist this procedure is trial-and-error and may require to take several time-consuming tomographies. Choosing the region of interest to large or to small will lead to additional time and costs with this method. This gives the main advantage of the proposed method based on hardness measurements, as it is easy and cheap to investigate even larger numbers of different hardness imprints for the estimation of the size of the RVE. The numerical simulation on the one hand and the determination of the relevant geometric parameters of the three-dimensional structure on the other hand serve as validation. The second topic of the work is the efficient numerical modeling based on the microstructure and its 3D tomographic representation. A data reduction approach based on material definition at the integration points of the finite element model is presented. The paper is structured as follows: In Sect. 2, the dual-phase steel under consideration in the study is presented and the experimental basics of the work, the tomography preparation and the process of performing the hardness measurements, are explained. Sect. 3 deals with the numerical implementation. In addition to the general FE implementation of the simulation, the developed data reduction method is described here. In Sect. 4 and Sect. 5, the results of the RVE size estimation and the data reduction are subsequently presented and evaluated. Sect. 6 summarizes the presented work and classifies it into the context of

modern microstructure-based simulations.

2 Material and experimental Methods

2.1 Dual-Phase steel

In this study a sample of a thermo-mechanically rolled dual-phase steel plate with a carbon content of approximately 0.06 $wt\%$ and a carbon equivalent of approximately 0.38 $wt\%$ was used. The microstructure consists of a ferritic matrix and a martensitic second phase. In Fig. 1 a light optical image using 500× resolution after modified Beraha etching according to (Britz et al. (2016)) and an electron microscopic image of one second phase object after electrolytic etching are shown. The second phase exhibits in an equiaxed shape, slightly stretched in rolling direction. The second phase objects in the electron microscopic image show a martensitic structure.

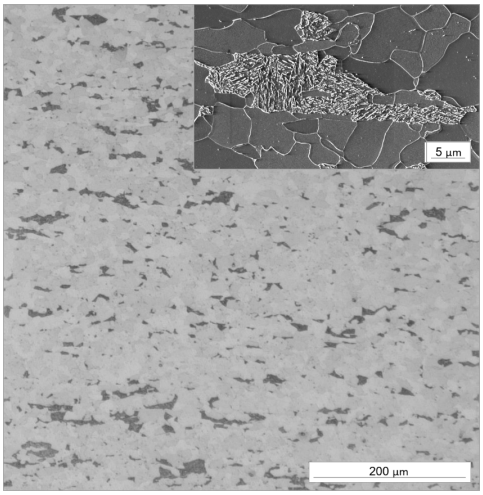

Figure 1: Light optical image of the Beraha etched sample with an electron microscopy image in the top right corner. In the light optical image, only the second phase is clearly contrasted (dark). In the SEM the substructure of the second phase becomes clear and also the grain boundaries of the ferrite are recognizable.

2.2 3D-Tomography

The setup presented by MÃijcklich et al. was used to produce a light microscopy serial sectioning tomography of the two-phase steel (Mücklich et al. (2015)). The tomography was performed on a modified setup based on a *Leica TXP* target preparation machine for the material removal and a digital light optical microscope (LOM) *VHX* 2000 for imaging. This allows a semi-automatic execution of the working steps in one setup. For the production of the tomography data the sample was first fixed to the sample holder of the *TXP* machine with the embedding material *DEMOTec*15+. Then the following steps polishing, etching and image acquisition were repeated several hundred times in order to obtain a representative volume. The material removal was performed using a neoprene cloth and the polish suspension *MasterPrep* with diamond particles in an average diameter of 0.05 µm was used within the *TXP* machine. The material removal per cut was adjusted by the contact pressure of 30 N, the rotation speed of the polishing disk of 400 RPM and the polishing time of 3 min using 2 ml polishing suspension. A modified Beraha etching according to Britz et al. was used to contrast the microstructure (Britz et al. (2016)). With this etching it is possible to contrast the second phase regions stronger than the grain boundaries of the ferritic matrix, so that an optical separation of the second phase regions from the matrix was achieved (Britz et al. (2016)).

Thus, the different phases in microscope images can be segmented by threshold and the images can be converted into binary images by means of image processing programs, Fig. 2. A 3D tomographic reconstruction of the microstructure is obtained by reconstructing the z-position of the binarized images. For the reconstruction of the volume there were 426 images with 424×928 pixels and a pixel size of 409 nm × 409 nm available after the pictures were taken. These pictures were first z-positioned with the program *Thermo Scientific Amira* ® and then aligned. The alignment of the images was done using fixed markings on the sample, which were placed on the sample before the tomography process. These markings were also used to determine the original z-position after the material removal per cut. The binary images were generated by threshold segmentation in *Amira*. For this standard filters like shading correction and denoising were used. Artifacts and errors as well as all objects that were only visible in one image were deleted using binary operations. To provide isotropic voxels for the reconstruction, the binary image stack was interpolated to a z distance of 409 nm. Fig. 3 shows the 3D reconstruction of the sample.

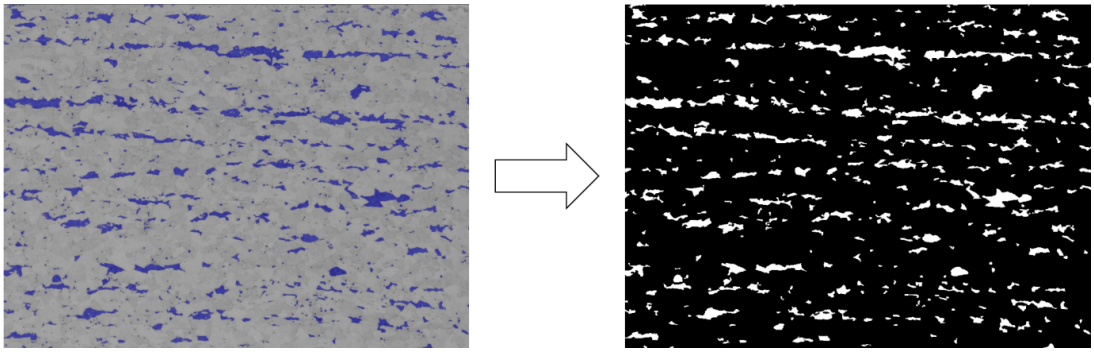

Figure 2: Exemplary representation of light optical images with selected second phase areas (left) and binary image after threshold segmentation (right) that is used for the reconstruction of the microstructure.

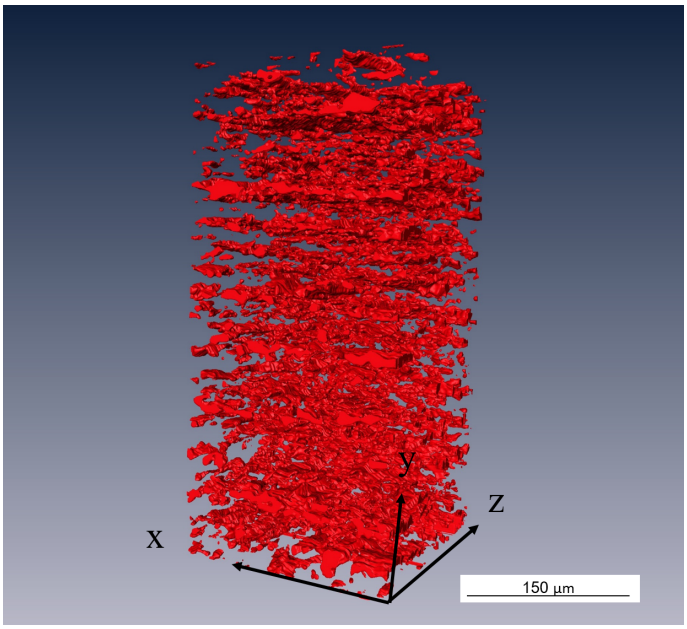

Figure 3: Visualization of the 3D reconstruction of the image stack.

2.3 3D parameter-based RVE size estimation

As an assumption, the 3D microstructure contains all necessary information about different structural components. Many parts of this 3D structure can be identified by determining parameters from 2D sections using stereological relationships (Ohser and Mücklich (2000)). However, parameters such as the connectivity of the phases can only be determined in 3D and a 2D analysis is not adequate, especially for such fissured phases. For this reason an evaluation of the RVE of the tomography was additionally determined by its 3D parameters. In order to find the RVE size cubic volume elements in different sizes were cropped and their characteristic 3D geometric parameters were measured using the program *Mavi*. For that purpose the parameters volume density, surface density, Euler density and particle density were examined for their spreading of the mean value. The quantities and their explanation are shown in Tab. 1. The first three quantities are implemented in *Mavi* and can be calculated from the fully reconstructed tomographies. For the particle density each individual second phase object in the set was counted and the number was divided by the whole volume. The Euler number from the Euler density is a measure of the connectivity of an object of a phase in a multi-phase material that consists of different objects. The calculation examines whether an object has a concave or convex curved surface or whether the surface is a saddle surface (Russ and Dehoff (2000)).
For the RVE estimation cubes with ten different edge lengths between 15 µm and 150 µm were selected. For each size four cubes are cropped from one large experimental data set and their 3D parameters were measured. The center point of the cubes remains at the same position for all sizes. For the estimation of the RVE, the mean value and the standard deviation of all 3D parameters were determined for the four cubes.

2.4 Indent-based RVE size estimation

In general, hardness describes the resistance of a material to the penetration by another object (Bargel et al. (2009)). In the present paper the hardness test according to Vickers (Bargel et al. (2009); Deutsches Institut für Normung (2006)) was used to estimate the RVE size. In the Vickers hardness measurement, an equilateral square diamond pyramid with an opening angle of 136° is pressed into the sample with a defined force F. After the unloading the diagonals d_1 and d_2 of the remaining imprint are

Table 1: Name and meaning of the volume-based parameters used for evaluation.

parameter	explanation
volume density	Ratio of the total volume of all second phase objects to the total volume of the tomography.
surface density	Ratio of the total surface of all second phase objects to the total surface of the tomography.
Euler density	Ratio of Euler number of the objects observed (difference between object number N and connectivity (object connections C)) to the total volume of the tomography
particle density	Ratio of the number of second phase objects to the total volume of the tomography.

measured and the hardness HV is determined to

$$HV = 2F \sin\left(\frac{136°}{2}\right)\left(\frac{2}{d_1 + d_2}\right)^2, \tag{1}$$

where F is given in kilopond, d_1 and d_2 in millimeters. When specifying the hardness value, the test force is given by default, e. g. 160 HV0.5 for a hardness value of 160, which was determined with a force of 0.5 kp. In theory, with varying test load used the imprint diameter changes while the hardness value remains constant (Strnad and Jakab-Farkas (2014)). Therefore, in the case of a completely homogeneous material, both very small and very large hardness imprints should result in the same hardness value with varying test loads.

Based on this assumption, a method for estimating the RVE size was developed in this study in order to overcome the disadvantages of the time-consuming methods described in Sect. 1. The functional principle is shown in Fig. 4. Each hardness imprint has a certain zone of influence, which is deformed by the imprint. A very small hardness imprint has correspondingly a very small zone of influence. Thus it is possible that the zone of influence lies entirely in a purely ferritic area or in a predominantly martensitic area of the microstructure. Due to this, very small hardness imprints show a high scattering in an inhomogeneous material. Above a certain indentation size, the zone of influence is just large enough to cover the size of an RVE. Starting from this indentation size, the spread of the hardness values decreases considerably, as a representative volume of the structure is examined at any time. In particular, the scattering for even larger imprints no longer decreases further, since a larger zone of influence contains no new microstructure information. Based on this hypothesis, a total of 121 hardness measurements were performed on the cross section[1] of the steel with loads ranging from 0.05 kp to 30 kp, see Tab. 2.

Table 2: Number of indents per load level

load [kp]	0.05	0.1	0.2	0.5	1	3	5	10	20	30
number [–]	36	25	16	9	16	9	4	4	1	1

The distance between two hardness imprints is chosen as at least three times the imprint diameter according to the norm for Vickers hardness measurements (Deutsches Institut für Normung (2006)).

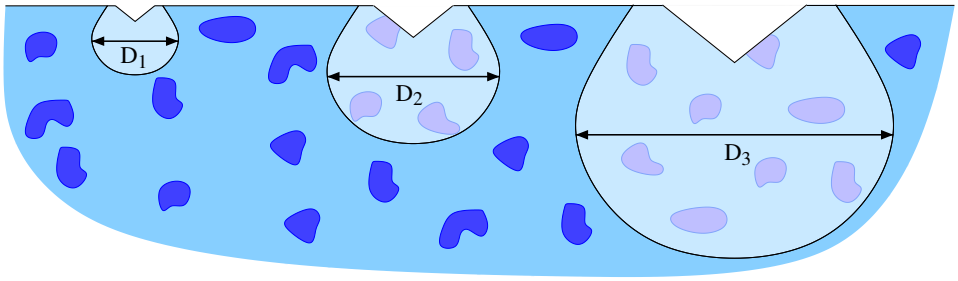

Figure 4: Schematic representation of three hardness imprints and their zones of influence. The size of the influence zone D is well below the RVE size on the left, in the middle in the area of the RVE size and well above it on the right.

3 Numerical Methods

Before the results of the methods for the estimation of the RVE size are discussed, an overview over the numerical methods used in the presented work are given in the following section. At first, the general implementation of the material behaviour in the context of FEM is explained. Then, the method developed for data reduction,i.e. material definition at the integration point, is presented.

[1] Section spanned by the transverse direction and the normal direction.

3.1 General numerical implementation

The material is described by an elastoplastic material model. In addition, the examination is focused on the small strain range. Hooke's law is used for the elastic part of the model. Consequently, the relation between the engineering stress $\boldsymbol{\sigma}$ and the engineering strain $\boldsymbol{\varepsilon}$ reads

$$\boldsymbol{\sigma} \;=\; 2\mu\,(\boldsymbol{\varepsilon} - \boldsymbol{\varepsilon}_p) + \lambda \mathrm{tr}\big(\boldsymbol{\varepsilon} - \boldsymbol{\varepsilon}_p\big)\,\mathbf{I}, \tag{2}$$

with the plastic part of the engineering strain $\boldsymbol{\varepsilon}_p$ and the Lamé parameters μ and λ. The plastic part model is described by a standard J_2 von Mises plasticity model (Mises (1913)) and isotropic, linear hardening. This results in a yield condition

$$g \;=\; \|\boldsymbol{\sigma}_\mathrm{D}\| - \sqrt{\frac{2}{3}}(\sigma_y - K\,\alpha), \tag{3}$$

with the deviatoric part $\boldsymbol{\sigma}_\mathrm{D}$ of the engineering stress tensor, the initial yield strength σ_y, the hardening modulus K and the flow parameter α. As small strains are considered, an additive decomposition of the strain tensor into its elastic and plastic part

$$\boldsymbol{\varepsilon} \;=\; \boldsymbol{\varepsilon}_e + \boldsymbol{\varepsilon}_p \tag{4}$$

is applied. The evolution of the plastic strain follows an associated flow rule

$$\dot{\boldsymbol{\varepsilon}}_p \;=\; \gamma\,\frac{\partial g}{\partial \boldsymbol{\sigma}}\,, \tag{5}$$

with the plastic multiplier γ.

The abovementioned material behaviour is implemented as an FEM model with the help of the open source C++ program library *deal.II* (Arndt et al. (2016); Bangerth et al. (2007)). Starting point is the balance of momentum for a body Ω with boundary Γ in its weak form in the stationary case

$$\int_\Omega \mathrm{grad}\,(\delta\mathbf{u}) : \boldsymbol{\sigma}(\mathbf{u})\;\mathrm{V} \;=\; \int_\Gamma \delta\mathbf{u}\cdot\mathbf{t}\;\mathrm{a}, \tag{6}$$

with the gradient operator $\mathrm{grad}\,(\cdot)$, the test function $\delta\mathbf{u}$ and the Neumann boundary condition $\mathbf{t}$. The solution is then iteratively calculated with Newton's method. In this context, a high variability of the implemented code with respect to possible extension is achieved by calculating the required derivation of the balance of momentum not analytically, but by means of a numerical tangent (Goldschmidt (2015); Scherff (2019); Scherff et al. (2016)). Plasticity is treated by the Radial Return Method (Bednarcyk et al. (2008); Simo and Taylor (1985); Simo and Hughes (2000); Wilkins (1963)). Finite differences are applied for the calculation of the derivative of the yield condition with respect to the plastic increment for the sake of variability.

Although the analysis is limited to small macroscopic strains, large strains can theoretically occur within the microstructure. Therefore, in a previous study (Scherff (2019)), a Neo-Hooke model for finite deformation was used to investigate whether this has an impact. As expected, within the microscopic stress field relative deviations between the small strain model and the large strain model of up to 10% were observed. Nevertheless it could be shown that the small strain model leads to negligibly small deviations well below 1% for the macroscopic stress-strain relationship under uniaxial tension. Therefore, the small strain model is applicable in the use case under consideration.

The parameters used for the single ferrite and martensite phase were determined with the help of nanoindentation tests, see Scherff (2019). They are given in Tab. 3. As shown in Scherff (2019), the simulation model described above is capable to reproduce the real behavior of the investigated dual-phase steel under uniaxial load with high accuracy.

Table 3: Material parameters used in this study for the ferrite and martensite phase.

	ferrite	martensite
μ [GPa]	89.5	91.7
λ [GPa]	173.7	141.0
K [GPa]	1.70	2.96
σ_y [MPa]	401	1081

3.2 Data reduction

As the microstructures under consideration in tomography consist of a very large number of voxels, many millions of degrees of freedom are generated in classical hexahedral meshing by assigning a single voxel to a single hexahedral element. As a result, the computing time required to solve the system and the memory required for storage increases immensely. Since such

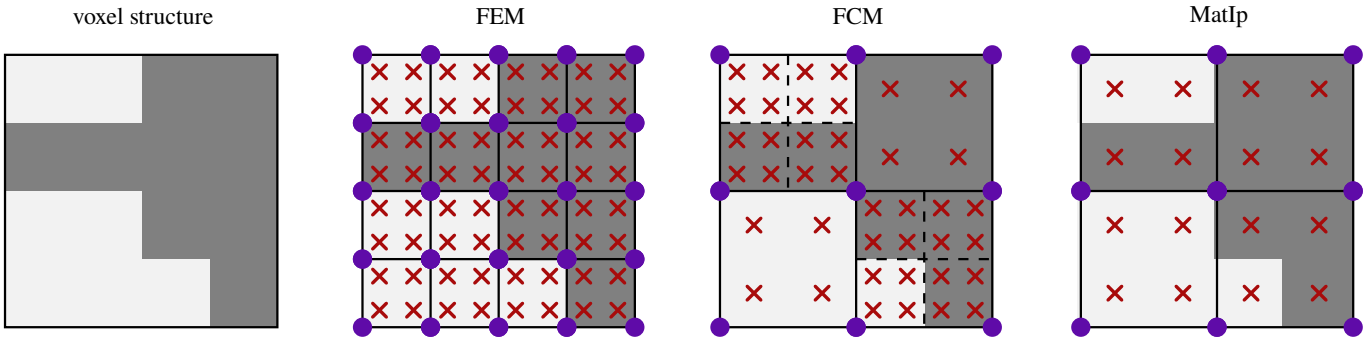

Figure 5: Meshing of a two-component voxel structure by classical FEM, FCM and MatIp (q2fe1). Element nodes are represented by violet dots, integration points by red crosses, element edges by black lines and sub-element edges of the FCM by dashed black lines.

calculations can usually no longer be carried out in an acceptable time on usual workstations, in addition to estimating the RVE size, data reduction is of great importance in the presented work. The aim is to reduce the required number of elements for meshing the microstructure, and thus computing time and working memory load, as far as possible, while maintaining all relevant structural information at the same time. Material definition at the integration point (MatIp) was used for this purpose. The idea of MatIp is based on Gauss Point Oversampling (Zohdi and Wriggers (2004)) and especially on the Finite Cell Method (FCM, (Düster et al. (2008); Parvizian et al. (2007))). The basic idea of FCM is to mesh the geometry under consideration in a strongly coarser way, so that several voxels are assigned to one element. The mesh then includes the geometry under consideration as well as parts of its surrounding. In order to integrate the system equation over these elements, sub-elements are introduced, which make it possible to carry out the integration over elements with homogeneous material. Inspired by this procedure, MatIp was implemented within the framework of this paper. Also in this case several voxels of the structure are combined to one element, whereby one voxel is assigned to exactly one integration point. Instead of standard Gaussian integration points, a grid of equidistant integration points, corresponding to the homogenous voxel size of the tomography, is applied. Accordingly, when calculating stress and treating plasticity, separate material parameters are used at each integration point, depending on whether it is a ferrite or martensite integration point. In contrast to FCM, it is not necessary to use sub-elements to integrate elements with mixed material. While complex geometries with homogeneous material are coarsened in the FCM including their surrounding, leading to a tensile strength of zero in parts of the mesh, good results are achieved with MatIp even with classical integration in comparison to the calculation in full resolution due to the relatively small differences in tensile strength between ferrite and martensite. Here, the order of the integration polynomials and the order of the shape functions can vary depending on the chosen method. For identification purposes, the number of integration points and the order of the shape functions are specified. For example q2fe1-MatIp means material definition at the integration point with linear shape function and two integration points per spatial direction in the element. In this case, one element corresponds to eight voxels of tomography. In order not to influence the volume fraction of martensite by unequal integration weights, equidistant integration points with constant weights were implemented. In Fig. 5 the difference between normal meshing, FCM and MatIp is schematically shown for a two-dimensional geometry. The shown MatIp meshing represents the entire microstructure in the FE mesh, while at the same time achieving a straightforward reduction in the number of elements and degrees of freedom. Further details of MatIp are discussed in Scherff (2019).

It is import to mention, that generally the FCM shows considerably good results with respect to convergence of the solution and accuracy of the results on the microscopic level (Düster et al. (2008); Parvizian et al. (2007)), even for complicated geometries and use cases. These advantages are, however, at the expense of complex and elaborate implementation. At this point the presented method shows its efficiency, with a straightforward and time saving implementation, for the investigated class of applications.

4 Results and Discussion - RVE Size

4.1 Experimental Results

The hardness measurements carried out result in the distribution shown in Fig. 6. As expected, the low hardness classes $HV0.05$ and $HV0.1$ with correspondingly small hardness imprints show a very high spread of the hardness values. From $HV0.2$ on, the spread drops significantly. For higher hardness classes, the spread remains at the same level. More precisely, the standard deviation of the hardness values of initially 20% decreases to under 3% starting with the $HV0.2$ imprint and the spread between maximum and minimum hardness decreases from 70% to under 9% of the mean value. Both values are within the range of measurement accuracy. Consequently, the RVE size is within the range of a $HV0.2$ imprint's zone of influence. The further reduction of the spread from $HV5$ upwards is mainly due to a reduced number of imprints due to the high size of the imprints, also see Tab. 2. A $HV0.2$ indentation corresponds to an imprint diameter of about $d_{\text{imprint}} = 50\,\mu\text{m}$ at the present mean hardness. However, the size of the zone of influence is not clearly defined, which prevents a clear statement on RVE size at this point. However, the minimum distance between two hardness imprints according to the norm (Deutsches Institut für Normung (2006)) offers a clue. To ensure that the influence zones of two indentations do not overlap, this distance is three times the indentation diameter, $d_{\text{norm}} = 3\,d_{\text{imprint}}$. The size of the influence zone therefore lies between a minimum edge length of one single imprint diameter and a maximum edge length of three times the imprint diameter, i.e. between 50 µm and 150 µm. This assumption is

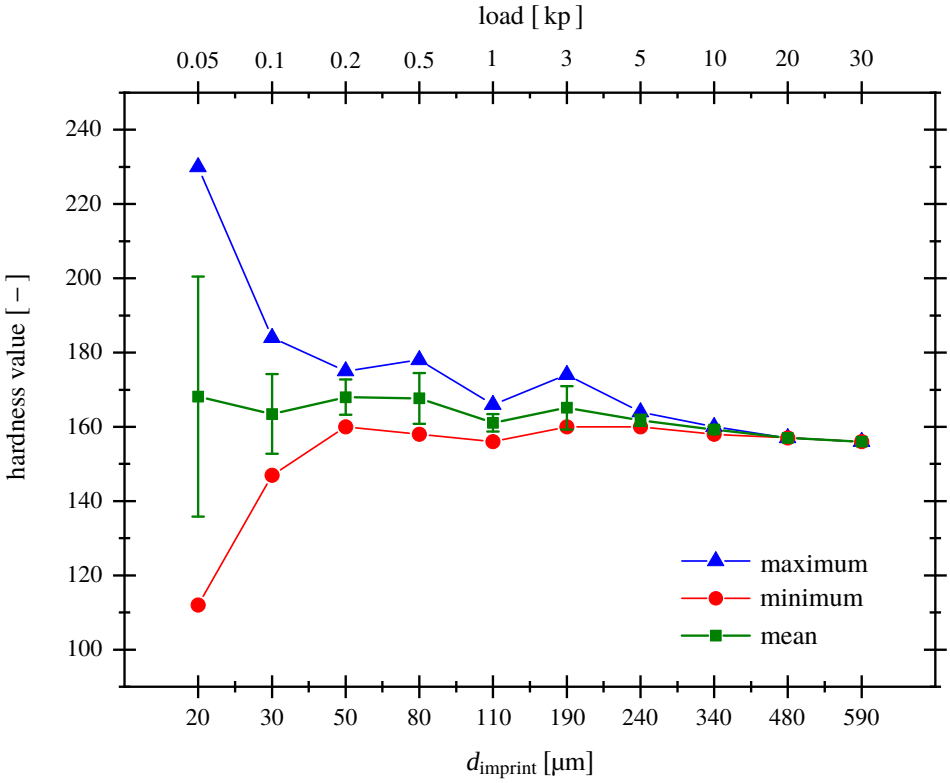

Figure 6: Maximum, minimum and mean value with standard deviation of the hardness values for different test loads.

evaluated below and the exact value is determined.

4.2 Evaluation of the RVE size estimation

To numerically evaluate the experimental RVE estimation, a tomography was prepared of a dual-phase steel, as shown in Sect. 2.2. Its size in each spatial direction is above the specified maximum RVE size of 150 µm edge length. The tomography is divided into smaller blocks of the same size and tensile tests are simulated on the individual blocks. The procedure is carried out for blocks with an edge length approximately in the range of the single, double and triple imprint diameter. The size classes thus cover the previously estimated RVE size range. Their extent is shown in Fig. 7 in relation to a two-dimensional section of the tomography. The edge lengths are 52 µm, 105 µm and 157 µm instead of 50 µm, 100 µm and 150 µm for reasons of efficient meshing[2]. Based on the simulations, the average stress value at 5% total strain $R_{t5.0}$ is determined for each block. The spread of $R_{t5.0}$ within a size class is then considered as a function of the block size. Fig. 8 shows a similar trend for $R_{t5.0}$ as Fig. 6 shows for the hardness. The spread of the hardness decreases much faster at the beginning, but the overall hardness also scatters more strongly than $R_{t5.0}$. The spread decreases from about 50 MPa for 52 µm edge length to less than 10 MPa for 157 µm edge length, which is in the range of real macroscopic tensile tests. Fig. 8 thus proves the assumption that the RVE size corresponds approximately to three times

[2]Due to the underlying data structure, meshes with edge lengths of $(x\,2^y)$ elements, with x as low as possible, can be better parallelized

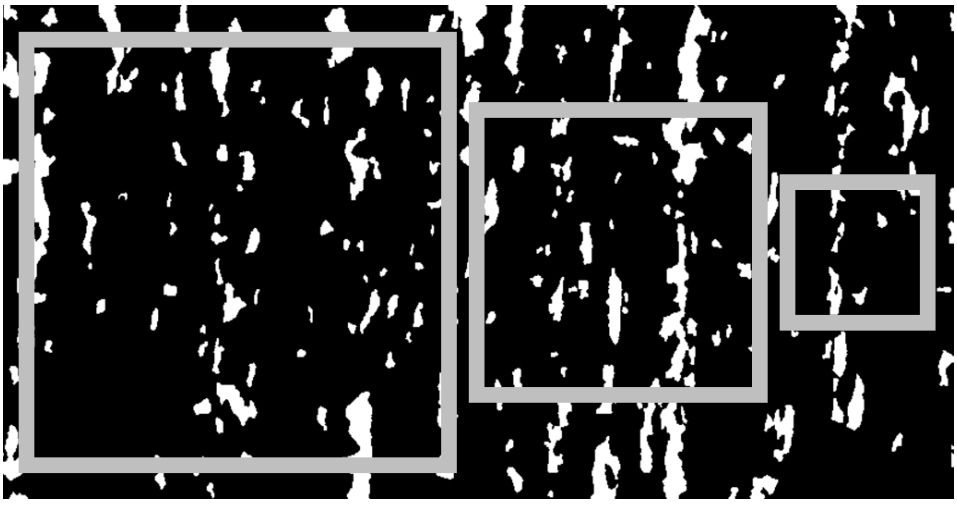

Figure 7: Two-dimensional representation of the three considered block sizes in comparison to the tomography.

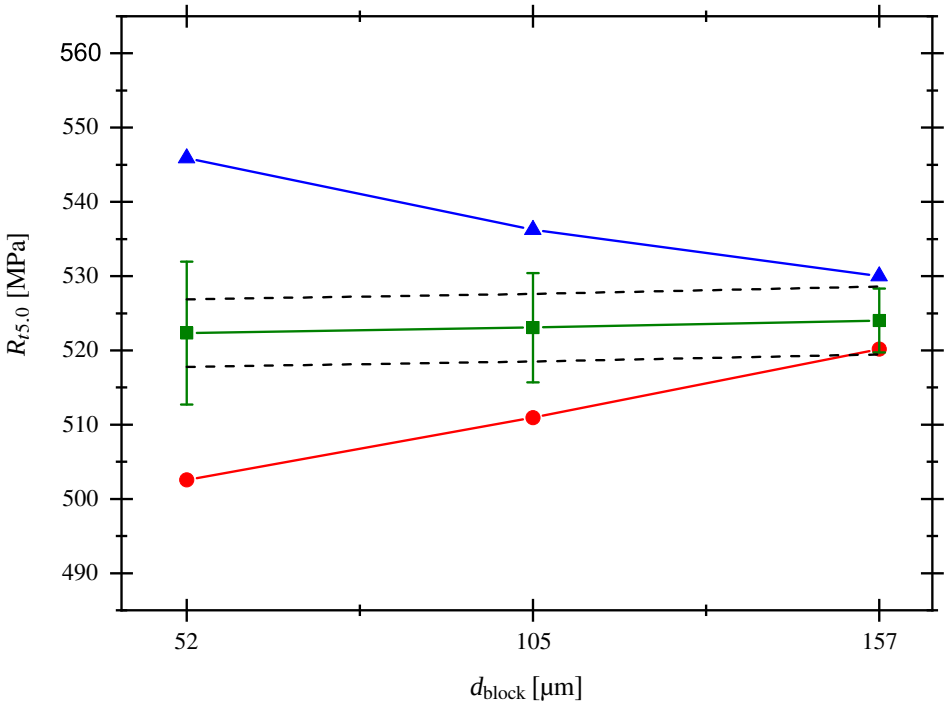

Figure 8: Maximum (blue), minimum (red) and mean value with standard deviation (green) of $R_{t5.0}$ for the different block sizes. The standard deviation of macroscopic tensile tests on the investigated steel is given in black.

the diameter of the hardness imprint for which the spread becomes sufficiently low. The investigated steel therefore has an RVE edge length of about 150 µm.

Fig. 8 shows another characteristic of the microstructure besides the validation of the RVE size estimation. The ensemble mean of the three size classes remains at approximately the same level. As a result, the structure studied is ergodic. In the context considered here, ergodicity means the equality of the ensemble mean of a property over a sufficiently large number of unrepresentatively small sections with the mean over a representative large volume (Ostoja-Starzewski (2007)). This leads to relevant advantages for the simulation and also for future tomographies. On the one hand, the required memory decreases significantly with sequential simulation of several small structures instead of one large structure, on the other hand, the experimental effort also decreases. Due to the ergodicity, it is not necessarily required to tomograph a coherent block in RVE size. A volume that contains a sufficient number of smaller blocks may be sufficient. However, this statement cannot easily be generalized to other microstructures. In particular for strongly heterogeneous microstructures or microstructures with very high connectivity of the second phase, it can be assumed that this statement does not apply or does only apply to a limited extent.

The RVE was additionally estimated using the 3D structural parameters as described in Sect. 2.3. The results are presented in Fig. 9. For small edge lengths a large spread of the 3D parameters can be seen. From approx. 80 µm edge length the spread remains at the same level for all four 3D parameters. This implies that the size of the RVE, with respect to the geometry, is in the range of 80 µm. The Euler density, which is a parameter for characterizing the connectivity, shows a constant profile from a slightly lower edge length of 60 µm on. However, to be sure that the volume is representative, all parameters should be considered at the same time. Thus the found result of the RVE-size based on 3D parameters corresponds to the RVE-size based on mechanical properties determined above, especially considering the generally higher relative spread of the geometry parameters.

5 Results and Discussion - Data Reduction

5.1 Impact of data reduction

In this section, the results of the implemented data reduction method are presented, both in terms of the reduction of computing time and memory usage as well as its accuracy. The load case here is always uniaxial tension in the transverse direction of the steel. The uniaxial tension test is considered here, as it is the universal standard test used in industry in this context, in contrast to other tests like shear, torsion or compression tests. To compare the variants of MatIp, finite elements with two, four, eight and sixteen integration points or voxels per spatial direction are considered. The number of integration points or voxels per spatial direction per element is referred to in the following as the reduction order. All simulations are performed with linear shape functions. The reduction orders 4 and 8 are additionally calculated with quadratic and cubic shape functions. To evaluate the reduction effect, a tensile test is simulated on one exemplary structural section. The section has an edge length of 52 µm or 128 vx and contains a total of 2, 097, 152 vx. During the simulation, the computing time and the memory utilization are recorded to compare the values. The goal in each case is to reduce the computing time and the memory utilization as much as possible without changing the result through the reduction. A full-resolution simulation with classical conforming hexahedral meshing

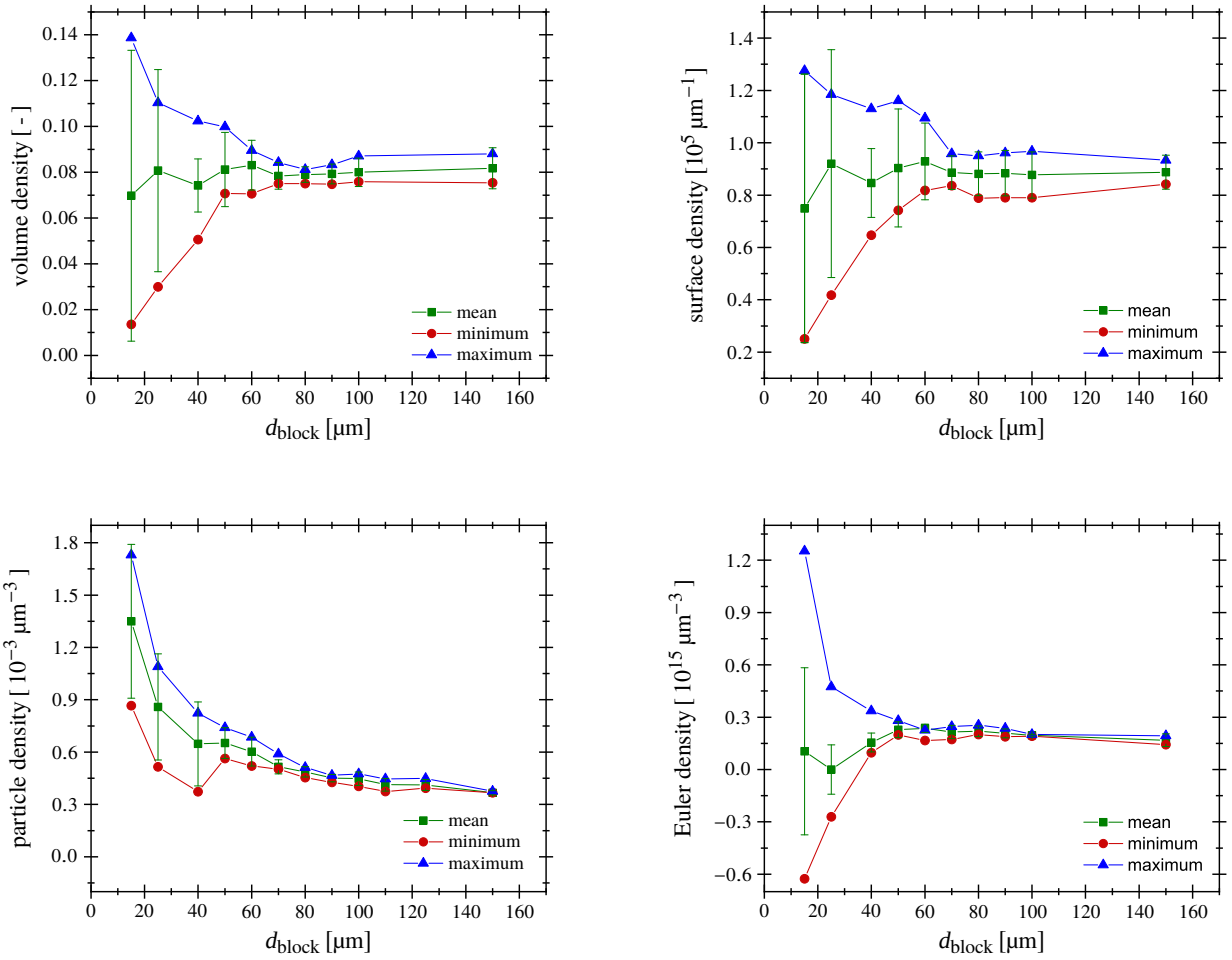

Figure 9: Maximum, minimum and mean value with standard deviation of the volume density (top left), surface density (top right), particle density (bottom left) and Euler density (bottom right) for different block sizes.

and linear shape functions serves as a reference.

Tab. 4 shows the computing time t_{sim}, the maximum memory usage l_m, the total number of degrees of freedom n_{dof} and the number of voxels per element n_{ve} of the different simulations. In the following, the term *element order* is used as an abbreviation for the order of the element's shape function. If the element order remains the same, the number of elements of the mesh and the number of degrees of freedom decrease with increasing order of reduction, resulting in a reduction of the computing time. At element order 1, the computing time decreases by a factor of 9 for the reduction order 2, for the reduction order 4 even by a factor of 34. For the reduction order 8 the computing time decreases only insignificantly, for the order 16 not at all anymore. The reason for this is that the quality of the approximation of the displacement field by the integration function drops considerably due to the high number of different integration points for higher reduction orders. This increases the computing time by a higher effort of time for the solution of the equation system. Memory usage shows a similar trend. Here, the memory load for the reduction orders 2 and 4 decreases by a factor of 7 and 12, respectively. For higher orders, the memory load even begins to increase slightly again. There are two reasons for this. On the one hand, the amount of data stored at the integration point remains constant, because the total number of integration points is not influenced by MatIp. Therefore, a plateau in the memory load is to be expected with increasing reduction order. On the other hand, the type of the underlying parallelization of the model in *deal.II* results in an increased memory load with high reduction orders. Each processor stores not only the data of the elements belonging to its domain, but also the data of all elements directly adjacent to it. With the large number of elements in full resolution or lower reduction orders, this doubling does not have much impact. In high reduction orders, however, there are only a few elements with a high number of integration points. Thus this element doubling has a strong influence and the memory load rises again starting from reduction order 8. A further trend that is evident, as expected, is that memory utilization and computing time increase with increasing element order at constant reduction order. Fig. 10 shows the stress strain diagrams for the simulations with different reduction orders compared to the simulation in full resolution. For a better comparison, Fig. 11 additionally shows the corresponding $R_{t5.0}$ values. MatIp leads, especially with a high reduction order of 8 or 16, to a certain virtual hardening of the material. The martensite integration points influence the element stiffness more strongly than desired. This effect is partly compensated by the additional degrees of freedom with higher order of approach, as can be seen from the course of $R_{t5.0}$ for the different variants of MatIp with reduction order 4 and 8. A preferred variant of MatIp can be determined

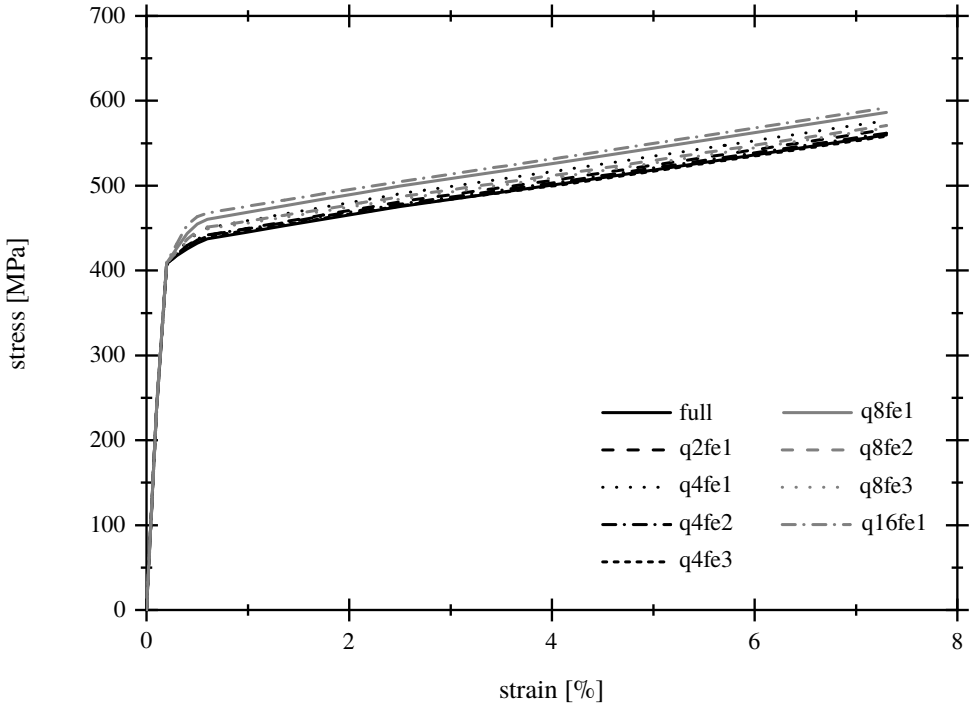

Figure 10: Stress strain diagrams for simulation in full resolution and various MatIp reduction orders.

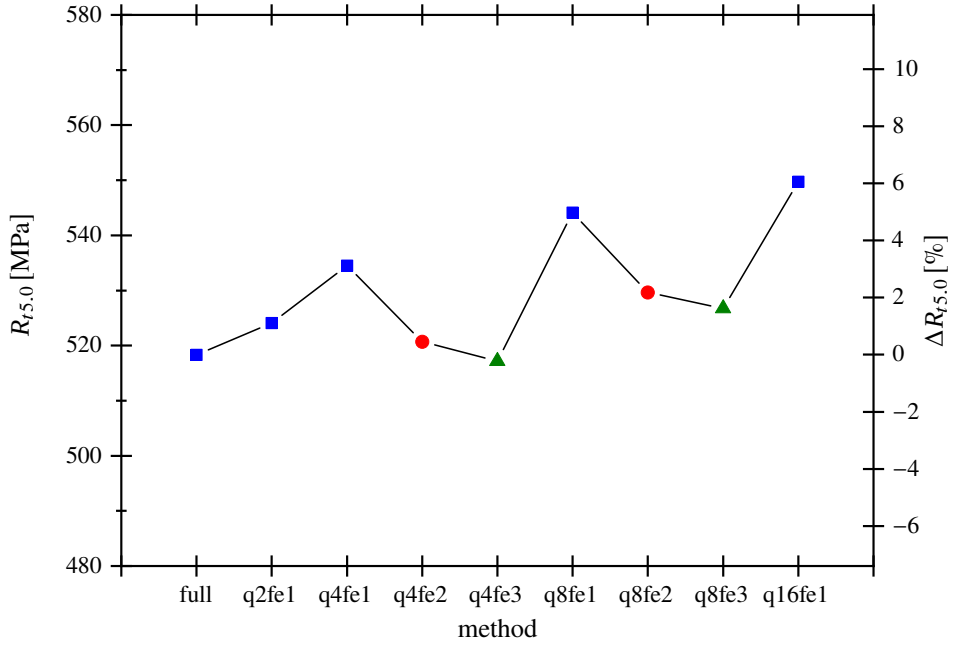

Figure 11: $R_{t5.0}$ for simulation in full resolution and various MatIp reduction orders. Different element orders are marked with different symbols and colors. The lines are given to illustrate the trend in $R_{t5.0}$, between the different reduction orders.

Table 4: Comparison of computing time, memory load, number of degrees of freedom and number of voxels per element for MatIp with the simulation in full resolution. In the term qXfe$Y$, X gives the reduction order and Y the order of the element's shape function.

	t_{sim} [min]	l_m [GB]	n_{dof} [−]	n_{ve} [−]
full resolution	286.7	34.3	6,440,067	1
q2fe1	32.3	4.9	823,875	8
q4fe1	8.4	2.8	107,811	64
q4fe2	74.4	6.9	823,875	64
q4fe3	648.8	28.2	2,738,019	64
q8fe1	5.9	3.4	14,739	512
q8fe2	27.6	3.9	107,811	512
q8fe3	127.0	6.6	352,947	512
q16fe1	5.9	5.5	2,187	4,096

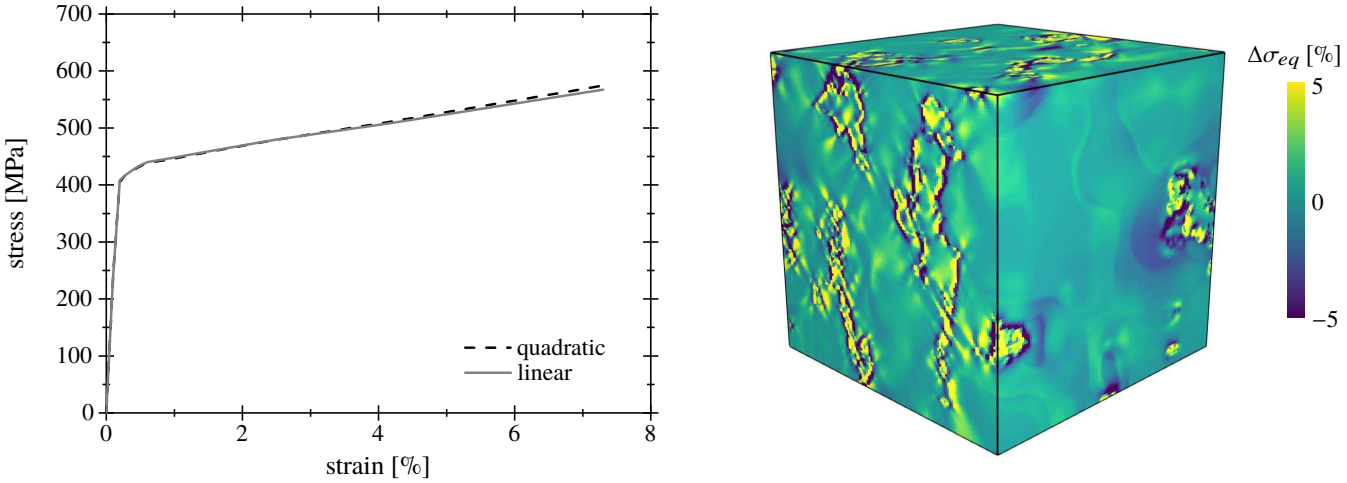

Figure 12: Stress strain diagram for a simulation with linear and quadratic shape functions (left) and the relative difference between the 3D von Mises equivalent stress fields at the end of the simulation (right). For the sake of visualization, the relative difference is limited to a range of ±5%.

by combined consideration of the mechanical behavior and the computing time. When considering the difference in the stress level, only the reduction orders 2 and 4 show a sufficiently small deviation. When on the other hand the calculation time is considered, the variants with a higher element order show themselves to be insufficient. This reduces the analysis to q2fe1 and q4fe1 as reduction methods. The variant q2fe1 has a stress value closer to the simulation in full resolution, but requires about four times the computing time of q4fe1. Since q4fe1 also generates only a small deviation of about 3%, this variant is considered the most reasonable solution for most use-cases, as this stress difference is in the range of the spread of normal uniaxial tension tests. However, depending on the application and the desired level of accuracy, q2fe1 can also be used effectively.

The present investigation is limited to the macroscopic level. Even if the deviations due to MatIp are small on the macroscopic level as shown here, local deviations may occur. These can be of importance in the initiation of cracks, for example if the model is extended to damage. For an analysis of the local deviations, see Scherff (2019) for details.

5.2 Verification

In the following, the developed data reduction method will be verified. This happens in two steps. Firstly, a simulation in full resolution with quadratic shape functions shows that the used reference is valid. Secondly, MatIp is compared with a simulation with a geometry conforming mesh.

In the discussions in Sect. 5.1 the result of the simulation in full resolution served as reference value. Each voxel was thus assigned to a linear hexahedral element of the mesh. However, since linear elements tend to locking effects, a further simulation was carried out. In this simulation, the structure was meshed with hexahedral finite elements with quadratic shape functions in the sense of p-refinement. The aim of this is the verification of the originally used reference simulation[3]. The results of this simulation are presented in Fig. 12 in comparison to the simulation with linear shape functions. When considering the stress strain diagrams, the two simulations show no relevant difference, for example the difference in $R_{t5.0}$ is 0.7%. Only at higher elongations

[3] As the simulation with quadratic shape functions produces a memory load of more than 300 GB, a high performance computing server was utilized instead of the workstation used in the rest of the work.

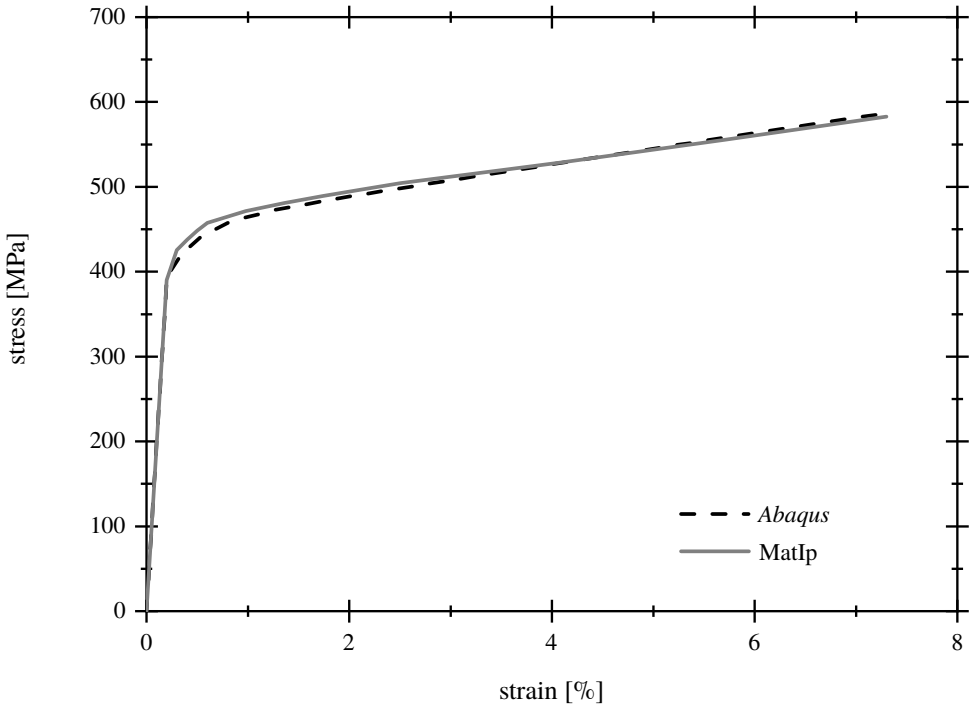

Figure 13: Stress strain diagram for a simulation with MatIp-*deal.II* and with *Abaqus*.

the curves begin to drift very slightly apart. If, however, the field of stress is considered in detail instead, this statement must be limited. Here, too, the difference between linear and quadratic shape functions is negligibly small for the majority of the structure. Around 95% of the structure shows a difference below 5%, more than 70% even a difference below 1%. However, a small area, especially the boundary layer between ferrite and martensite, shows relevant differences. These differences range for a few elements up to almost 55%. Overall, these outliers have no influence on the final result in the macroscopic stress strain diagram. In the context considered in this paper, with the stress strain diagram as target and with an elastic-plastic material model, the simulation with linear shape functions is therefore a valid reference. Limitations must, however, be placed on that conclusion to the extent that the differences observed in the microstructure may be of significance in future investigations. Especially when considering damage effects, they can serve as crack initiators. But since the principal distribution of the stress maxima in linear and quadratic calculations is still identical and only their height differs, the influence cannot yet be estimated.

As mentioned in Sect. 1, the geometry conforming meshing of microstructures is also an option. For this purpose, a section with 96 vx edge length of the considered microstructure was meshed with tetrahedral elements using the program *Simpleware ScanIP*®, a software package for three-dimensional image processing and segmentation of tomographies. In the sense of an efficient simulation, the 884, 736 vx of the tomography could be meshed with about 320, 000 tetrahedral elements through structure smoothing. Since the simulation program based on *deal.II* used in this paper is only designed for hexahedral elements, the geometry conforming mesh was investigated in a simulation with *Simulia Abaqus FEA*®. The result is then compared with a simulation with MatIp. Thus, in addition to comparing the types of meshing, this study also compares the developed FE code with an established commercial FE program. The other parameters of the simulation, like material model, material parameters and boundary conditions, were chosen in *Abaqus* analogous to the self-developed code implemented in *deal.II*. The resulting stress-strain diagrams of the two simulations are shown in Fig. 13. The two stress strain diagrams show a very large accordance. The only difference is a small deviation at the start of yield, otherwise both curves are approximately identically. In addition, both simulations required approximately the same computing time per CPU core. This shows a significant secondary advantage of the implemented FE code with MatIp compared to the commercial program *Abaqus*. The parallelized open source implementation allows the use of any number of processor cores[4]. The license model of *Abaqus* also allows an arbitrarily high level of parallelization, but in real-world use it is generally limited due to the number of licenses owned. Overall, the result of the implemented simulation routine and meshing method can thus be verified and its advantage over commercial FEM software can be shown.

6 Conclusion

Two important points for the efficient and realistic microstructure-based simulation of dual-phase steel were implemented in the paper. On the one hand, a straightforward experimental method for estimating the size of the RVE was established, and, on the other hand, MatIp was developed as a method for efficient meshing of microstructures.

A large number of hardness measurements with different test loads and thus different imprint diameters were carried out. With

[4]For the utilized program library *deal.II* linear scaling of parallelization is shown for calculations with more than 16, 000 CPU cores (Bangerth et al. (2012))

the hypothesis that the spread of these hardness values strongly decreases for indentation diameters whose influence zone lies in the range of the RVE size, the RVE size of the dual-phase steel under consideration with regard to the mechanical properties could be estimated to about 150 µm for the investigated dual-phase steel. Based on this, a 3D tomography was prepared and sections of different sizes were examined. Numerical simulations on these sections were able to prove the estimated RVE size. Similarly, the investigation of the geometric parameters of the microstructure revealed an RVE size with respect to the geometric parameters in the same size range. Hence, by comparing the proposed method with two other established methods for determining the RVE size, we could confirm our assumptions, at least for the class of material under consideration in this study.

Since microstructures usually consist of millions of voxels, a method for data reduction in hexahedral meshing was developed. By defining the material at the integration point instead of for each element as a whole, the simulation time could be reduced by a factor of 30 and the memory load by a factor of 12 compared to the full resolution simulation. To verify the simulation, a comparison simulation with p-refinement and a simulation of a geometry conforming mesh of the structure were performed. Both showed a high agreement to the simulation with MatIp.

The RVE size estimation now makes it possible to determine the appropriate size of a tomography before it is produced, thus simplifying the manufacturing process. A microstructure determined in this way can then be meshed by MatIp and used for the realistic and very efficient simulation of dual-phase steel on the basis of its microstructure. Further investigations on the suitability of the implemented simulation process and MatIp in consideration of damage effects will have to be carried out in the future.

Acknowledgment

The authors thank Prof. Dr. Dietrich Klakow and his department *Sprach- und Signalverarbeitung* at *Universität des Saarlandes* for readily providing access to his high performance computing server for the calculation of the simulation described in Sect. 5.2.

References

J. Alkemper and P. W. Voorhees. Quantitative serial sectioning analysis. *Journal of Microscopy*, 201(3):388–394, 2001.

D. Arndt, W. Bangerth, D. Davydov, T. Heister, L. Heltai, M. Kronbichler, M. Maier, J.-P. Pelteret, B. Turcksin, and D. Wells. The deal.II library, version 8.5. *J. Num. Math.*, 24:135–141, 2016.

W. Bangerth, R. Hartmann, and G. Kanschat. deal.II – a General Purpose Object Oriented Finite Element Library. *ACM Trans. Math. Softw.*, 33(4):24/1–24/27, 2007.

W. Bangerth, C. Burstedde, T. Heister, and M. Kronbichler. Algorithms and Data Structures for Massively Parallel Generic Adaptive Finite Element Codes. *ACM Trans. Math. Softw.*, 38(2):14:1–14:28, 2012.

H. Bargel, P. Cardinal, H. Hilbrans, G. Schulze, and G. Wurzel. *Werkstoffkunde*. Springer-Lehrbuch. Springer, 2009.

M. B. Bauza, J. Tenboer, M. Li, A. Lisovich, J. Zhou, D. Pratt, J. Edwards, H. Zhang, C. Turch, and R. Knebel. Realization of Industry 4.0 with high speed CT in high volume production. *CIRP Journal of Manufacturing Science and Technology*, 22: 121–125, 2018.

B. Bednarcyk, J. Aboudi, and S. Arnold. The equivalence of the radial return and Mendelson methods for integrating the classical plasticity equations. *Computational Mechanics*, 41(5):733–737, 2008.

D. Brands, D. Balzani, L. Scheunemann, J. Schröder, H. Richter, and D. Raabe. Computational modeling of dual-phase steels based on representative three-dimensional microstructures obtained from EBSD data. *Archive of Applied Mechanics*, 86(3): 575–598, Mar 2016.

D. Britz, A. Hegetschweiler, M. Roberts, and F. Mücklich. Reproducible Surface Contrasting and Orientation Correlation of Low-Carbon Steels by Time-Resolved Beraha Color Etching. *Materials Performance and Characterization*, 5(5):553–563, 2016.

T. Burnett, R. Kelley, B. Winiarski, L. Contreras, M. Daly, A. Gholinia, M. Burke, and P. Withers. Large volume serial section tomography by xe plasma fib dual beam microscopy. *Ultramicroscopy*, 161:119 – 129, 2016.

T. M. Buzug. *Computed Tomography: From Photon Statistics to Modern Cone-Beam CT*. Springer Berlin Heidelberg, 2008.

M. Calcagnotto, D. Ponge, E. Demir, and D. Raabe. Orientation gradients and geometrically necessary dislocations in ultrafine grained dual-phase steels studied by 2D and 3D EBSD. *Materials Science and Engineering: A*, 527(10):2738–2746, 2010.

D. Das and P. P. Chattopadhyay. Influence of martensite morphology on the work-hardening behavior of high strength ferrite-martensite dual-phase steel. *Journal of Materials Science*, 44:2957–2965, 06 2009.

R. G. Davies. Influence of martensite composition and content on the properties of dual phase steels. *Metallurgical Transactions A*, 9(5):671–679, May 1978.

F. Desplentere, S. Lomov, D. Woerdeman, I. Verpoest, M. Wevers, and A. Bogdanovich. Micro-CT characterization of variability in 3D textile architecture. *Composites Science and Technology*, 65(13):1920–1930, 2005.

Deutsches Institut für Normung. Metallische Werkstoffe – Härteprüfung nach Vickers. DIN EN ISO 6507, Berlin, 2006.

M. Diehl, P. Shanthraj, P. Eisenlohr, and F. Roters. Neighborhood influences on stress and strain partitioning in dual-phase microstructures. *Meccanica*, 51(2):429–441, Feb 2016.

H.-F. Dong, J. Li, Y. Zhang, J. Park, and Q.-X. Yang. Numerical simulation on the microstress and microstrain of low Si-Mn-Nb dual-phase steel. *International Journal of Minerals, Metallurgy, and Materials*, 17(2):173–178, Apr 2010.

A. Düster, J. Parvizian, Z. Yang, and E. Rank. The finite cell method for three-dimensional problems of solid mechanics. *Computer Methods in Applied Mechanics and Engineering*, 197(45-48):3768–3782, 2008.

M. Echlin and T. Pollock. Femtosecond Laser Serial Sectioning: A New Tomographic Technique. In *8th. World Congress on Computational Mechanics*, 2008.

M. Fischer, A. Stieben, H. Quade, and W. Bleck. 3D Metallography of a Multiphase steel. In *Tagungsband zum 26. Aachener Stahlkolloquium – Werkstofftechnik*, pages 37–48, 2011.

F. Goldschmidt. *Modellierung und Simulation von Klebeverbindungen mit gradierten mechanischen Eigenschaften*. PhD thesis, Universität des Saarlandes, Saarbrücken, 2015.

R. Hill. Elastic properties of reinforced solids: Some theoretical principles. *Journal of the Mechanics and Physics of Solids*, 11 (5):357–372, 1963.

N. Ishikawa, K. Yasuda, H. Sueyoshi, S. Endo, H. Ikeda, T. Morikawa, and K. Higashida. Microscopic deformation and strain hardening analysis of ferrite-bainite dual-phase steels using micro-grid method. *Acta Materialia*, 97:257–268, 2015.

L. K. Ji, H. L. Li, H. T. Wang, J. M. Zhang, W. Z. Zhao, H. Y. Chen, Y. Li, and Q. Chi. Influence of Dual-Phase Microstructures on the Properties of High Strength Grade Line Pipes. *Journal of Materials Engineering and Performance*, 23(11):3867–3874, Nov 2014.

J. Kadkhodapour, A. Butz, S. Ziaei-Rad, and S. Schmauder. A micro mechanical study on failure initiation of dual phase steels under tension using single crystal plasticity model. *International Journal of Plasticity*, 27(7):1103–1125, 2011.

J. Kang, Y. Ososkov, J. D. Embury, and D. S. Wilkinson. Digital image correlation studies for microscopic strain distribution and damage in dual phase steels. *Scripta Materialia*, 56(11):999–1002, 2007.

T. Kanit, S. Forest, I. Galliet, V. Mounoury, and D. Jeulin. Determination of the size of the representative volume element for random composites: Statistical and numerical approach. *International Journal of Solids and Structures*, 40(13-14):3647–3679, 2003.

S. Katani, S. Ziaei-Rad, N. Nouri, N. Saeidi, J. Kadkhodapour, N. Torabian, and S. Schmauder. Microstructure Modelling of Dual-Phase Steel Using SEM Micrographs and Voronoi Polycrystal Models. *Metallography, Microstructure, and Analysis*, 2 (3):156–169, Jun 2013.

E. Keehan, L. Karlsson, H. K. D. H. Bhadeshia, and M. Thuvander. Three-dimensional analysis of coalesced bainite using FIB tomography. *Materials Characterisation*, 59:877–822, 01 2008.

S. Kim and S. Lee. Effects of martensite morphology and volume fraction on quasi-static and dynamic deformation behavior of dual-phase steels. *Metallurgical and Materials Transactions A*, 31(7):1753–1760, Jul 2000.

F. Lasagni, A. Lasagni, E. Marks, C. Holzapfel, F. Mücklich, and H. Degischer. Three-dimensional characterization of 'as-cast' and solution-treated AlSi12(Sr) alloys by high-resolution FIB tomography. *Acta Materialia*, 55(11):3875–3882, 2007.

M. Li, S. Ghosh, T. N. Rouns, H. Weiland, O. Richmond, and W. Hunt. Serial Sectioning Method in the Construction of 3-D Microstructures for Particle-Reinforced MMCs. *Materials Characterization*, 41(2):81–95, 1998.

R. Li, X. Zuo, Y. Hu, Z. Wang, and D. Hu. Microstructure and properties of pipeline steel with a ferrite/martensite dual-phase microstructure. *Materials Characterization*, 62(8):801–806, 2011.

M. Marvi-Mashhadi, M. Mazinani, and A. Rezaee-Bazzaz. FEM modeling of the flow curves and failure modes of dual phase steels with different martensite volume fractions using actual microstructure as the representative volume. *Computational Materials Science*, 65:197–202, 2012.

R. v. Mises. Mechanik der festen Körper im plastisch-deformablen Zustand. *Nachrichten von der Gesellschaft der Wissenschaften zu Göttingen, Mathematisch-Physikalische Klasse*, 1913:582–592, 1913.

F. Mücklich, M. Engstler, D. Britz, J. Barrirero, and P. Rossi. Why we need all dimensions to solve both very old and very new questions in materials at the micro-, nano-and atomic scales. *Practical Metallography*, 52(9):507–524, 2015.

F. Mücklich, M. Engstler, D. Britz, and J. Gola. Serial Sectioning Techniques – a Versatile Method for Three-Dimensional Microstructural Imaging. *Practical Metallography*, 55(8):569–578, 2018.

J. Ohser and F. Mücklich. *Statistical Analysis of Microstructures in Materials Science*. John Wiley & Sons, 2000.

M. Ostoja-Starzewski. *Microstructural randomness and scaling in mechanics of materials*. Chapman and Hall, 2007.

J. Parvizian, A. Düster, and E. Rank. Finite cell method: h- and p-extension for embedded domain problems in solid mechanics. *Computational Mechanics*, 41(1):121–133, 2007.

S. K. Paul. Real microstructure based micromechanical model to simulate microstructural level deformation behavior and failure initiation in DP 590 steel. *Materials & Design*, 44:397–406, 2013.

PlasticsEurope. Weltweite und europäische Produktionsmenge von Kunststoff in den Jahren von 1950 bis 2016 (in Millionen Tonnen). `https://de.statista.com/statistik/daten/studie/167099/umfrage/weltproduktion-von-kunststoff-seit-1950/`, 2017. (05.11.2018).

A. Ramazani, K. Mukherjee, H. Quade, U. Prahl, and W. Bleck. Correlation between 2D and 3D flow curve modelling of DP steels using a microstructure-based RVE approach. *Materials Science and Engineering: A*, 560:129–139, 2013.

A. Ramazani, Z. Ebrahimi, and U. Prahl. Study the effect of martensite banding on the failure initiation in dual-phase steel. *Computational Materials Science*, 87:241–247, 2014.

M. Roland, A. Kruglova, G. Gaiselmann, T. Brereton, V. Schmidt, F. Mücklich, and S. Diebels. Numerical simulation and comparison of a real Al–Si alloy with virtually generated alloys. *Archive of Applied Mechanics*, 85(8):1161–1171, Aug 2015.

J. C. Russ and R. T. Dehoff. *Practical Stereology*. Springer US, 2000.

F. Scherff. *Modellierung der Gefüge-Eigenschafts-Korrelation bei Dualphasenstahl*. PhD thesis, Universität des Saarlandes, Saarbrücken, 2019.

F. Scherff, F. Goldschmidt, S. Scholl, and S. Diebels. High-resolution simulation of microstructures in dual-phase steel. *PAMM*, 16(1):391–392, 2016.

J. Simo and R. Taylor. Consistent tangent operators for rate-independent elastoplasticity. *Computer Methods in Applied Mechanics and Engineering*, 48(1):101–118, 1985.

J. C. Simo and T. J. Hughes. *Computational Inelasticity*, volume 7 of *Interdisciplinary applied mathematics*. Springer Science & Business Media, 2000.

G. Strnad and L. Jakab-Farkas. Improving the accuracy of low-load Vickers microhardness testing of hard thin films. *Procedia Technology*, 12:289–294, 2014.

V. Tarigopula, O. Hopperstad, M. Langseth, A. Clausen, and F. Hild. A study of localisation in dual-phase high-strength steels under dynamic loading using digital image correlation and FE analysis. *International Journal of Solids and Structures*, 45(2): 601–619, 2008.

C. Tasan, M. Diehl, D. Yan, C. Zambaldi, P. Shanthraj, F. Roters, and D. Raabe. Integrated experimental–simulation analysis of stress and strain partitioning in multiphase alloys. *Acta Materialia*, 81:386–400, 2014a.

C. Tasan, J. Hoefnagels, M. Diehl, D. Yan, F. Roters, and D. Raabe. Strain localization and damage in dual phase steels investigated by coupled in-situ deformation experiments and crystal plasticity simulations. *International Journal of Plasticity*, 63:198–210, 2014b. Deformation Tensors in Material Modeling in Honor of Prof. Otto T. Bruhns.

C. Tasan, M. Diehl, D. Yan, M. Bechtold, F. Roters, L. Schemmann, C. Zheng, N. Peranio, D. Ponge, M. Koyama, K. Tsuzaki, and D. Raabe. An Overview of Dual-Phase Steels: Advances in Microstructure-Oriented Processing and Micromechanically Guided Design. *Annual Review of Materials Research*, 45(1):391–431, 2015.

M. Uchic, M. Groeber, M. Shah, P. Callahan, A. Shiveley, M. Scott, M. Chapman, and J. Spowart. An Automated Multi-Modal Serial Sectioning System for Characterization of Grain-Scale Microstructures in Engineering Materials. In M. De Graef, H. F. Poulsen, A. Lewis, J. Simmons, and G. Spanos, editors, *Proceedings of the 1st International Conference on 3D Materials Science*, pages 195–202, Cham, 2016. Springer International Publishing. ISBN 978-3-319-48762-5.

M. L. Wilkins. Calculation of elastic-plastic flow. Technical report, California Univ Livermore Radiation Lab, 1963.

C. Yan, L. Hao, A. Hussein, P. Young, and D. Raymont. Advanced lightweight 316L stainless steel cellular lattice structures fabricated via selective laser melting. *Materials & Design*, 55:533–541, 2014.

A. Zeghadi, F. N'guyen, S. Forest, A.-F. Gourgues, and O. Bouaziz. Ensemble averaging stress–strain fields in polycrystalline aggregates with a constrained surface microstructure – Part 1: anisotropic elastic behaviour. *Philosophical Magazine*, 87(8-9): 1401–1424, 2007.

X. Zhong, M. G. Burke, P. J. Withers, X. Zhang, X. Zhou, T. L. Burnett, Y. Liu, S. B. Lyon, and S. R. Gibbon. Multi-modal plasma focused ion beam serial section tomography of an organic paint coating. *Ultramicroscopy*, 197:1 – 10, 2019.

H. Zhou, C. Li, L. Zhang, B. Crawford, A. S. Milani, and F. K. Ko. Micro-XCT analysis of damage mechanisms in 3D circular braided composite tubes under transverse impact. *Composites Science and Technology*, 155:91–99, 2018.

O. C. Zienkiewicz and R. L. Taylor. *The finite element method*, volume 36. McGraw-Hill London, 1977.

T. Zohdi and P. Wriggers. *Introduction to Computational Micromechanics (Lecture Notes in Applied and Computational Mechanics)*. Springer-Verlag, Berlin, Heidelberg, 2004.